Chapter 5
Contribution of the Numerical Approach to Kelvin Probe Force Microscopy on the Atomic-Scale

Laurent Nony, Franck Bocquet, Adam S. Foster, and Christian Loppacher

Abstract The goal of this chapter is to gather and detail recent numerical developments addressing the issue of atomic-scale measurements in Kelvin Probe Force Microscopy (KPFM). It is argued why the problem requires the combination between the atomistic description of the distance- and bias voltage-dependent force field occurring between the tip and the surface, as well as an accurate numerical implementation of the complex noncontact atomic force microscopy and KPFM setup. When combining these tools, it is possible to draw conclusions regarding the origin of the atomic-scale KPFM contrast and its connections with usual physical observables such as the surface potential and the local work function. These aspects are discussed with respect to the surface of a bulk ionic crystal.

5.1 Atomic-Scale Contrast in KPFM: Relevance of the Numerical Approach

Over the past decade, the combination between *non-contact Atomic Force Microscopy* (nc-AFM) and *Kelvin Probe Force Microscopy* (KPFM) [1, 2] has attracted much interest owing to the unique capability of the latter method to map the

L. Nony (✉) · F. Bocquet · C. Loppacher
Aix-Marseille Université, IM2NP, Centre scientifique de Saint-Jérôme, Avenue Escadrille Normandie-Niemen, Case 151, 13397 Marseille, CEDEX 20, France

CNRS, IM2NP (UMR 6242), Marseille-Toulon, France
e-mail: laurent.nony@im2np.fr

A.S. Foster
Department of Physics, Tampere University of Technology, P.O. Box 692, 33101 Tampere, Finland

Department of Applied Physics, Aalto School of Science, P.O. Box 1100, 02015 Helsinki, Finland
e-mail: adam.foster@tut.fi

spatial distribution of electrostatic forces down to the nanometer scale. Electrostatic forces occur between the nanoscopic tip of the AFM and the sample, henceforth referred to as the electrodes, as soon as they are electrically connected. They stem from intrinsic work function differences between the electrodes when they do not consist of similar materials and/or when they carry charges. They are usually interpreted on the macroscopic level as capacitive forces and are known to influence the nc-AFM operating mode [3–6]. The KPFM controller supplies the proper DC voltage that aligns the Fermi levels of both electrodes, thereby compensating the electrostatic force. Thus, the KPFM provides the *Contact Potential Difference* (CPD) between the electrodes. Hence, beyond the regular nc-AFM channels, i.e., topography and dissipation, the combined nc-AFM/KPFM setup allows also for the simultaneous acquisition of a CPD image.

In the early stages of its development, KPFM proved its ability to map the spatial variations of the CPD on the nanometer scale with a resolution of few millivolts [7–9]. With the goal in mind to understand better the connection between the structural and the electrical properties of the investigated samples on the atomic-scale, some research groups reported outstanding results with atomically resolved CPD images [2, 10–19]. KPFM has also been used as a way to map the chemical identity of surface atoms [13]. Surprisingly, the latter work is the earliest experimental attempt dealing with atomic-scale chemical identification by KPFM, though the topic has been intensively addressed by other experimental strategies based on site-specific force vs. distance measurements [20–25]. So far, atomic-scale KPFM contrast was reported on semiconducting surfaces: $Si(111)7 \times 7$ [10, 12, 15], $Si(111)5\sqrt{3} \times 5\sqrt{3}$-Sb [13], GaAs(110) [11] and InSb(001) [16], and on two bulk dielectric surfaces: $TiO_2(110)$ [17, 18] and KBr(001) [19]. In Figs. 5.1a, b and 5.1c, d are shown two examples of experimental results showing the simultaneous topographical-CPD atomic-scale contrast on the 7×7 Si(111) reconstruction [12] and on the KBr(001) surface [19], respectively.

Among the former references however, despite the consistency between the lateral periodicity of the CPD and topographical images, the CPD values neither fit the values reported by macroscopic methods, notably UV photoemission spectroscopy, nor the theoretical predictions [2, 10, 12]. Besides, it is now well stated that, when measured in the range of few angstroms up to 1–2 nm above the surface, the CPD varies with the tip-surface separation [14, 16, 26, 27]. These results are all the more surprising in that, when not used on the atomic-scale, i.e., down to a regime where the features at the surface have a size larger or similar to the size of the tip, KPFM provides CPD values that are compliant with the expected work function of the material [4, 8, 26, 28–34], the latter being not supposed to depend on the distance between the electrodes.

The experimental aspects of atomically resolved CPD images are not the scope of this chapter as these are presented in Chap. 13. However, it is interesting to point out some of their main findings. For instance, on the complex $Si(111)5\sqrt{3} \times 5\sqrt{3}$-Sb surface, Okamoto et al. concluded that the CPD images mainly reflect the electrostatic force distribution rather than the work function distribution [13, 14].
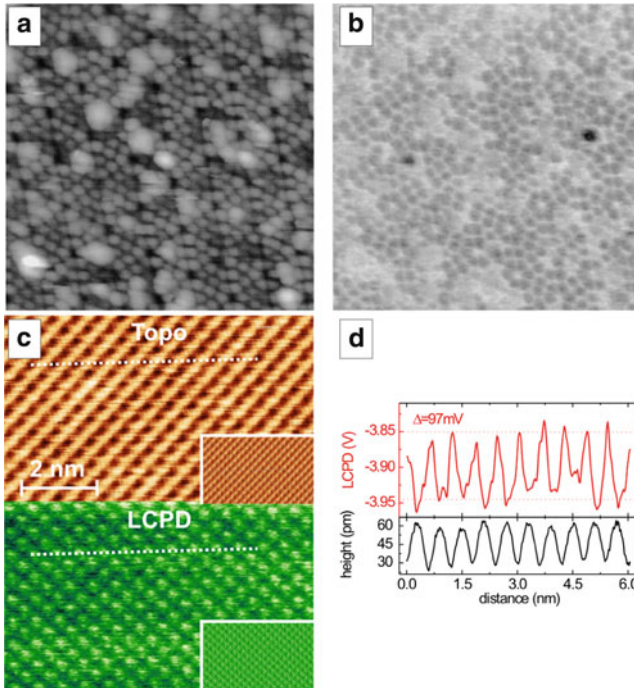
Fig. 5.1 Simultaneously acquired (**a**) topographical and (**b**) CPD nc-AFM images of a *p*-type Si(111)7 × 7 surface with deposited Au clusters. The atomic-scale contrast is well visible in both channels. The scan size is 20×20 nm². The vertical contrast of the CPD image ranges from −40 mV down to −180 mV and is brighter (larger CPD) on the Au clusters than on the adatoms of the 7 × 7 structure. Courtesy from [12]. (**c**) Simultaneously acquired topographical (*top*) and local CPD (LCPD, *bottom*) nc-AFM images of the KBr(001) surface. The insets show the corresponding error signals of the distance and KPFM controllers. The LCPD vertical contrast ranges from −3.95 to −3.85 V, corresponding to a contrast magnitude of 0.1 V. The magnitude of the topographical contrast is 30 pm only. Courtesy from [19]. (**d**) LCPD and topographical cross sections corresponding to the *dotted lines* shown in (**c**) showing the consistency between the atomic-scale topography and Kelvin contrast

On the Au/Si(111)7 × 7 surface, Kitamura et al. came also to the conclusion that the CPD does not reflect the work function of the observed atomic structures (see Fig. 5.1a, b), but rather the local electron density [12].

The discrepancy between the CPD values on the atomic-scale and the expected ones, as well as its unexpected distance dependence ultimately made KPFM measurements controversial and evoked questions of the origin and the relevance of the atomic-scale resolution in KPFM. What is the observable the technique provides access to: local work function, local surface potential, local surface charge density? Is the measurement quantitative? Why is the CPD distance dependent? Then, is it influenced by the distance regulator of the nc-AFM setup? The above elements can be rationalized as follows:

- When measured close to the surface, the CPD acquires a local character. Hence, the so-called *local CPD* (LCPD) must differ from its long-range value because the work function, well defined on the macroscopic scale, differs from the *local work function* on the atomic scale. The latter concept was introduced by Wandelt [35] to account for the fluctuations of the surface potential of real surfaces owing to fluctuations of the local density of states, presence of chemical and/or structural defects, steps, trapped charges, etc. Therefore, the discrepancy between CPD and LCPD was, to some extent, predictable.
- Since the KPFM technique is primarily sensitive to electrostatic forces, the atomic-scale CPD contrast relies on *Short-Range and bias dependent electrostatic forces* (SRE forces).

Two groups have initiated studies on the contribution of SRE forces in KPFM at this point [16, 19]. In a recent series of papers [19, 36], Bocquet et al. have described a self-consistent analytical approach to the LCPD probed by KPFM on the (001) facet of a bulk alkali halide single crystal. The approach, based on classical electrodynamics, relies on the estimate of the SRE force between a biased metallic tip and a semi-infinite dielectric slab. The analytic expression of the force allowed them to derive an expression of the LCPD. Although useful to understand the most important concepts of the problem, the analytical approach has two major drawbacks: (1) the tip must be restricted to a simple geometry and (2) deriving an expression of the LCPD requires an analytical description of the KPFM setup. This is only feasible with strong approximations. Therefore, the predicted values of the LCPD are hardly comparable to the experimental data, which ultimately restricts the relevance, as well as the accuracy of the analysis.

Following the experimental development of the nc-AFM technique, numerical methods such as ab initio and classical atomistic calculations have been developed by several groups to compute the distance dependence of short-range chemical forces for a wide set of realistic tips and surfaces [20–22, 37–44]. These methods brought a valuable gain to the nc-AFM technique as it is now possible to quantify the experimental images in terms of force and thus identify the interaction processes driving the atomic-scale topography contrast formation. Beyond the accurate description of the tip–surface interaction, numerical approaches tend to open new routes to the experimentalists such as chemical identification [20–22, 24, 25], dissipation processes [45–48], electron transfer processes [49], atomic or molecular manipulation [50–54], atomic or molecular diffusion barriers [51, 55, 56].

Following the works by Nony et al., atomistic calculations have been used to address the issue of SRE forces in the particular case of a bulk ionic sample [57]. However, when dealing with the nc-AFM/KPFM technique, the force field between the tip and the surface cannot be connected to the topography or LCPD contrast directly. It is also required to understand how the dynamics of the cantilever is changed when vibrating close to the surface under the dual influence of bias-dependent and non- bias-dependent interaction forces, that is actually the whole acquisition chain of the experimental setup. As said before, this is hardly feasible on the analytical level. Therefore, owing to the overall complexity of the tip–surface

interaction and the one of the nc-AFM/KPFM technique, a thorough analysis requires a combined numerical approach of the force field between the tip and the surface and of the experimental setup. This is the unique way to interpret the experimental results with the best accuracy. Thus, issues such as the origin and the quantitative character of the KPFM contrast on the atomic-scale can be addressed in details, while preventing imaging artifacts from occurring.

This chapter deals with recent developments of the numerical implementation of the two well-established KPFM setups, namely *Frequency Modulation-* and *Amplitude Modulation-KPFM* (FM- and AM-KPFM, respectively), coupled to atomistic simulations of the distance- and bias-dependent interaction force between a realistic tip and the (001) facet of a bulk single crystal of NaCl. The elements detailed hereafter are gathered in a set of three recent articles [19, 36, 57]. The implementation of the KPFM setups is performed within the core of an accurate numerical implementation of an existing nc-AFM setup, the so-called *nc-AFM simulator* [58], briefly described in Sect. 5.2. The connection between the simulator and FM- or AM-KPFM methods is described in Sect. 5.3. In Sect. 5.4, the atomistic simulations of the interaction force field between the NaCl crystal and a metallic tip including an ionic cluster in the topmost position will be presented. The use of the numerical force field as an input parameter of the nc-AFM/KPFM simulator allows for the simulation of spectroscopic measurements and topography and CPD images. The results will be discussed in Sect. 5.5. In Sect. 5.6, we will conclude by stressing the influence of the dynamic polarization of the ions at the tip–surface interface, which will allow us to draw conclusions concerning the relevance of the local CPD and its connection with physical observables such as the Madelung surface potential of the ionic crystal.

5.2 Prerequisite: The nc-AFM Simulator

To date, five groups have reported the implementation and/or performance of "virtual force microscopes" [58–63]. These simulation codes are almost analogous to ours, but differ in detail. Historically, our virtual instrument has been referred to as the nc-AFM simulator. It is a numerical implementation of an existing nc-AFM setup based on a *Phase-Locked-Loop-* (PLL-) excitation scheme [64]. Its original implementation is reported in Fig. 5.2. A simplified version is sketched in Fig. 5.3a, b. The PLL-excitation scheme consists in using the PLL to generate the time-dependent phase of the excitation signal of the cantilever. The PLL output is driven by the AC deflection signal of the cantilever and phase-locked to it, provided that the PLL settings are properly adjusted. Then the PLL continuously tracks the interaction-shifted resonance frequency of the cantilever $\widetilde{f}_0$ with high precision, whatever the tip-surface separation. One of the primary goals of the nc-AFM simulator was to address the issue of apparent dissipation (or apparent damping), that is of spurious variations in the driving amplitude caused by the nonlinear interaction occurring between the tip and the surface and by the finite response times of the various controllers (cf. section IV in [58]).
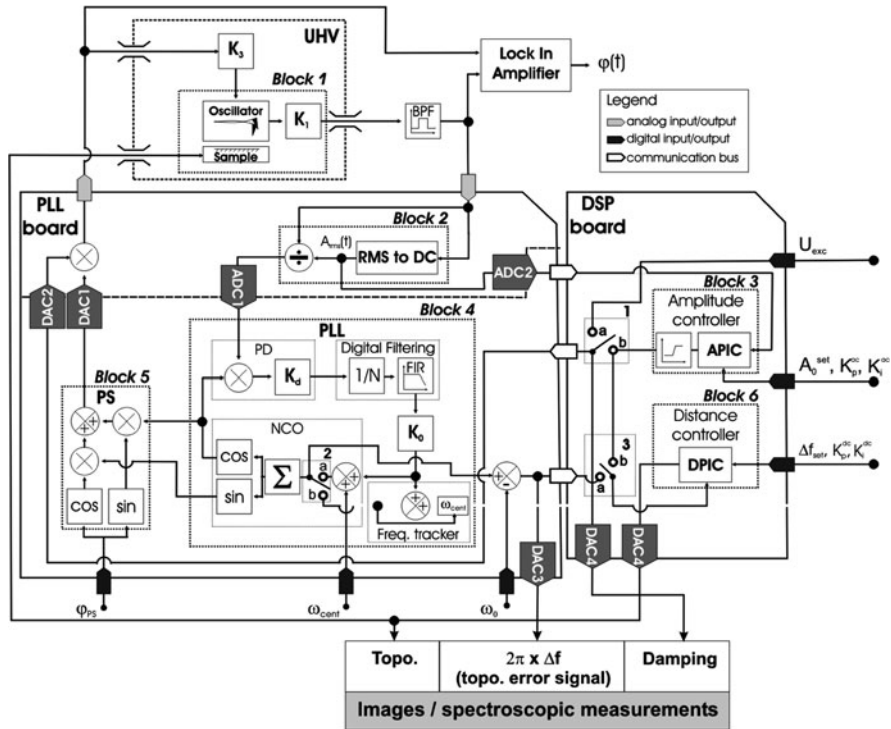
Fig. 5.2 Scheme of the numerical implementation of the nc-AFM simulator based on a real nc-AFM setup
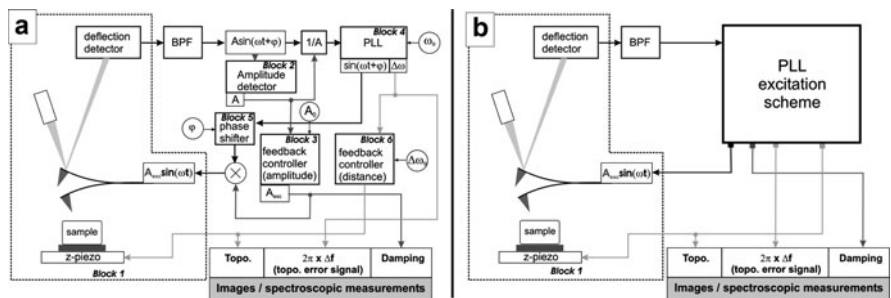

Fig. 5.3 (**a**) Simplified scheme of the nc-AFM simulator. The main features of the implementation are drawn. The PLL-excitation scheme ensures the continuous on-resonance driving of the cantilever while optimizing the quality of the driving signal. (**b**) Simplified scheme of the PLL-excitation scheme that is used for the KPFM implementation as discussed in Sect. 5.3

This section is built as follows: in Sects. 5.2.1 and 5.2.2, the numerical schemes of the blocks describing the dynamics of the cantilever and the *Lock-In Amplifier* (LIA) used to monitor the phase lag of the cantilever with respect to its excitation are detailed. They are indeed useful to understand the implementation of the KPFM setups. The numerical implementation of the PLL and the *proportional/integral controllers* (PIC) is not described here, but the equations ruling out their behavior are given in [58]. In Sect. 5.2.3, a brief summary of the main results obtained with the nc-AFM simulator is given.

5.2.1 Overview of the Numerical Implementation

The electronics of the simulated nc-AFM setup consists of analog and digital circuits described by six interconnected main blocks operating at various sampling frequencies (f_s), as sketched in Fig. 5.2. The highest sampling frequency among the digital blocks is the PLL one, $f_{s_1} = 20\,\text{MHz}$. The PLL electronics has initially been developed by Loppacher et al. [64]. Details regarding the operating mode of analog and digital PLLs can be found in the book by Best [65] for instance.

Block 1 in Fig. 5.2 mimics the detection of the vibration of the tip when interacting with the surface. In the simulation, the block is described by an equivalent analog circuit. More generally, all the analog parts of the electronics are described in the simulation using a larger sampling frequency compared to f_{s_1}, namely $f_{s_2} = 400\,\text{MHz}$. This is motivated by the ultrahigh vacuum environment within which the microscope is placed, thus resulting in a high quality factor of the cantilever, typically $Q = 30{,}000$ at room temperature. Besides, nc-AFM cantilevers have typical fundamental eigenfrequencies $f_0 \simeq 150\,\text{kHz}$. The chosen sampling frequency insures a proper integration of the differential equations minimizing the error. The signal of the oscillating cantilever then goes into a bandpass filter which cuts off its low and high frequency components. The bandwidth of the filter is typically 60 kHz, centered on the resonance frequency of the cantilever. Despite the implementation of a filter in the simulation, no noise has been introduced. The signal is then sent to other blocks depicting the interconnected parts of two boards, namely an analog/digital one, the "PLL board," and a fully digital one integrating a Digital Signal Processor (DSP), the "DSP board." The boards share data *via* a "communication bus" operating at $f_{s_3} = 10\,\text{kHz}$, the lowest frequency of the digital electronics.

Block 2 stands for the mere analog part of the PLL board ($f_s = f_{s_2}$). It is an RMS-to-DC converter, the output of which is the root mean square (RMS) value of the oscillation amplitude of the cantilever, $A_{\text{RMS}}(t)$. $A_{\text{RMS}}(t)$ is provided to block 3, one of the two PIC implemented on the DSP ($f_s = f_{s_3}$). When operating in the nc-AFM mode, the block output is the DC value of the driving amplitude that maintains constant the reference value of the oscillation amplitude, A_0^{set}. This is why it is referred to as the amplitude controller, APIC.

The dashed line in Fig. 5.2 depicts the border between analog and digital circuits in the PLL board. The digital PLL, block 4 ($f_s = f_{s_1}$), consists of three sub-blocks: a Phase Detector (PD), a Numerical Controlled Oscillator (NCO) and a filtering stage consisting of a decimation filter and a finite impulse response (FIR) low-pass filter in series. The PLL receives the signal of the oscillation divided by $A_{RMS}(t)$ plus an external parameter: the "center frequency," $f_{cent} = \omega_{cent}/2\pi$. f_{cent} specifies the frequency to which the input signal has to be compared for the demodulation frequency stage. The NCO generates the digital sin and cos waveforms of the time-dependent phase, ideally identical to the one of the input signal. The latter waveforms are then sent to a digital *phase shifter* (PS, block 5, $f_s = f_{s_1}$) that shifts the incoming phase by a constant amount, set by the user to maximize the oscillation amplitude of the cantilever, i.e., actually to ensure its on-resonance excitation. The block output is converted into an analog signal and then multiplied by the APIC output, thus generating the full AC excitation applied to the piezoelectric actuator to drive the cantilever on resonance.

Block 6 is the second PIC of the DSP ($f_s = f_{s_3}$). It controls the tip-surface separation to maintain constant either a given value of the frequency shift, or a given value of the driving amplitude (switch 3 set to location "a" or "b" in Fig. 5.2), respectively. The output is the so-called "topography" signal. The block is referred to as the distance controller, DPIC. In this work, the topography images have been calculated in the constant frequency shift mode (switch 3 set to location "a").

Finally, a digital LIA detects the phase lag, φ, between the excitation signal provided to the oscillator and the oscillating cantilever motion.

All the processed signals are properly converted by means of Analog-to-Digital or Digital-to-Analog Converters (ADC or DAC, respectively), the nominal bandwidths of which are much larger than the communication bus one. Therefore, although sketched in the figure, they are not implemented in the code of the simulator.

5.2.2 Numerical Schemes

5.2.2.1 Block 1: Cantilever and Optical Detection

The block mimics the photosensitive detector (PSD) acquiring the signal of the vibration of the cantilever. The equation describing its behavior is given by the differential equation of the harmonic oscillator:

$$\ddot{z}_0(t) + \frac{\omega_0}{Q_0}\dot{z}_0(t) + \omega_0^2 z_0(t) = \omega_0^2 \varXi_{exc}(t) + \frac{\omega_0^2}{k_0}\left[F_{int}(z) + F_{es}(V_b, z)\right] \qquad (5.1)$$

$\omega_0 = 2\pi f_0$, Q, k_0 stand for the angular resonance frequency, quality factor and stiffness of the fundamental bending eigenmode of the free cantilever, respectively. $z_0(t)$ and $\varXi_{exc}(t)$ are the instantaneous location of the tip with respect to the rest position of the cantilever (cf. Fig. 5.4a) and the excitation signal driving the
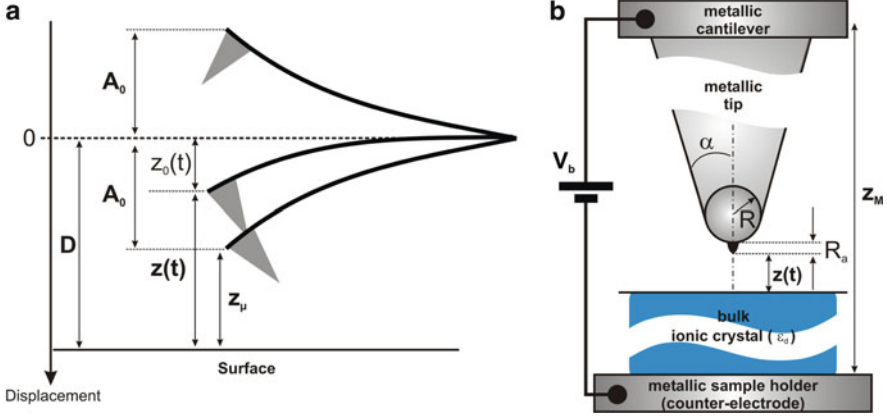
Fig. 5.4 (**a**) Geometrical parameters used for the description of the instantaneous position of the tip with respect to the surface. The tip is sketched for pedagogical purpose. (**b**) Actual geometry of the tip used in the simulations. The body of the tip is a cone with an open half-angle α. Its apex consists in a sphere with a radius R and a small cluster in topmost position protruding with a height R_a from the sphere. The dielectric ionic crystal below the tip is several millimeters thick

cantilever, respectively. $F_{\text{int}}(z)$ and $F_{\text{es}}(V_b, z)$ are the non-bias- dependent and bias-dependent (V_b) interaction forces acting between the tip and the surface, respectively. They primarily depend on the instantaneous tip-surface separation $z(t)$, connected to $z_0(t)$ and to the separation between the surface and the cantilever at rest, D (cf. Fig. 5.4a):

$$z(t) = D - z_0(t). \tag{5.2}$$

$z(t)$ is to be distinguished from the minimum tip-surface separation, referred to as z_μ in the following. z_μ stands for the position of the lower turning point of the oscillation of the cantilever with respect to the surface:

$$z_\mu = D - A_0, \tag{5.3}$$

where A_0 is the oscillation amplitude of the cantilever (cf. Fig. 5.4a).

$F_{\text{int}}(z)$ gathers long-range Van der Waals interactions and chemical short-range ones, and $F_{\text{es}}(V_b, z)$ gathers long-range and short-range electrostatic interactions. In the simulations, we have considered a long-range electrostatic force as a phenomenological force that consists of capacitive effects between the cantilever and the sample holder when mounted in the microscope. Van der Waals and long-range electrostatic interactions are implemented via common analytical forms (cf. equ. (2.4) in [66] and equ. (14) in [36], respectively):

$$F_{\text{int}}^{\text{vdW}}(z) = -\frac{H}{6}\left[\frac{R}{(z+R_a)^2} + \frac{\tan(\alpha)^2}{z+R_a+R'} - \frac{R'}{(z+R_a)^2 + z + R_a + R'}\right] \tag{5.4}$$

and:

$$F_{es}^{lr}(V_b, z) = -\frac{\epsilon_0 \epsilon_d^2 S V_b^2}{2(z + R_a + z_M)^2} \qquad (5.5)$$

R, R_a, α and $R' = R(1 - \sin\alpha)$ are the geometrical parameters for the tip, as sketched in Fig. 5.4b. H, ϵ_0 and ϵ_d are the Hamaker constant of the tip-surface interface, vacuum and sample dielectric permittivities, respectively. S and z_M are the effective area involved in the capacitive coupling between the cantilever and the counter-electrode and the corresponding distance between the electrodes, respectively. In the problem addressed here, the sample is a bulk dielectric that is several millimeters high. A quick estimate for $S = 1\,mm^2$, $z_M = 5\,mm$ and $V_b = 1\,V$ yields $F_{es}^{lr} \simeq -3\,pN$.

When using the nc-AFM simulator with atomistic force fields, a lookup table of the force values is built as a function of the tip-surface separation and the applied bias voltage, the size of which depends on the sampling rates of the tip-surface separation and of the bias voltage. By definition, it consists of the chemical and electrostatic short-range interactions. The total interaction force used to perform the simulations is then built for each value of the tip-surface separation and each value of the bias voltage as the sum between the latter short-range contributions and both long-range contributions derived from the former analytical expressions.

The differential equation is solved with a modified Verlet algorithm, so-called leapfrog algorithm [67], using a time step $\Delta t_{s_2} = 1/f_{s_2} = 5\,ns$. The instantaneous value of the driving amplitude $\Xi_{exc}(t)$ (units: m, cf. equ. (5.1)) can be written as:

$$\Xi_{exc}(t) = K_3 A_{exc}(t) z_{ps}(t) \qquad (5.6)$$

K_3 (units: m V^{-1}) stands for the linear transfer function of the piezoelectric actuator driving the cantilever. $A_{exc}(t)$ (units: V) is the APIC output. $z_{ps}(t)$ is the AC part of the excitation signal. It is provided by the phase shifter when the PLL is engaged. When the steady state is reached, i.e. $t \gg t_{steady} \simeq 2Q/f_0$, the block output has the form:

$$K_1 z_0(t) = K_1 A_0(t) \sin[\omega t + \varphi_0(t)]. \qquad (5.7)$$

K_1 (V m^{-1}) depicts the transfer function of the PSD, which is assumed to be linear within the bandwidth (3 MHz in the real setup). If the damping is kept constant, the amplitude and the phase, $A_0(t)$ and $\varphi_0(t)$, respectively, remain constant as well. This is no longer true once the controllers are engaged. This is why the time dependence has been explicitly preserved in the above equation.

5.2.2.2 Lock-In Amplifier

The simulated LIA does not mimic the detailed operational mode of the real dual phase lock-in that is used to monitor the phase shift of the oscillator (Perkin Elmer 7280). Its purpose is rather to provide a simple way to estimate the phase shift

between the excitation and the oscillation. In particular, the built-in low-pass filter has been simulated as a simple averaging analog circuit, but the bandwidth of the LIA remains adjustable. For monitoring the cantilever phase lag, it has been set equal to 2.5 kHz. The reference signal of the LIA is the driving signal of the cantilever with a time-dependent phase of the form ωt. The input signal of the LIA is the output of the bandpass filter z_{bpf}, i.e., a signal that is almost similar to the input of the filter owing to its wide band. The numerical code used to describe in- and off-phase components,[1] X_{LIA} and Y_{LIA}, respectively, is:

$$X_{\text{LIA}}(t) = \frac{\sum_{k=i-n_{\text{LIA}}}^{i} z_{\text{bpf}}(t_k) \times \sin(\omega t)}{n_{\text{LIA}}}$$

$$Y_{\text{LIA}}(t) = \frac{\sum_{k=i-n_{\text{LIA}}}^{i} z_{\text{bpf}}(t_k) \times \cos(\omega t)}{n_{\text{LIA}}}. \tag{5.8}$$

Hence, the phase of the oscillator with respect to the driving excitation is given by:

$$\tan(\varphi(t)) = \frac{X_{\text{LIA}}}{Y_{\text{LIA}}}, \tag{5.9}$$

while the vibration amplitude of the cantilever can also be derived as:

$$A_{\text{LIA}} = 2\sqrt{X_{\text{LIA}}^2 + Y_{\text{LIA}}^2}. \tag{5.10}$$

The LIA that is used in the KPFM setup is implemented with the same code, but with proper input, bandwidth, and reference signals.

5.2.2.3 Code Implementation

The numerical implementation has been performed in ANSI C. The integro-differential equations (5.1) and (5.6) are integrated at their respective sampling frequencies. The monitored signals are the oscillation amplitude A_0 given by the RMS-to-DC converter, the frequency shift Δf given by the PLL, the phase φ given by the LIA (5.9) and the relative damping $QK_3 A_{\text{exc}}/A_0 - 1$, deduced from the APIC output.

---

[1]In- and off-phase components of the LIA are essentially defined upon the structure of its input signal, i.e., here the driving signal of the cantilever which is arbitrarily generated out of a sinus waveform.
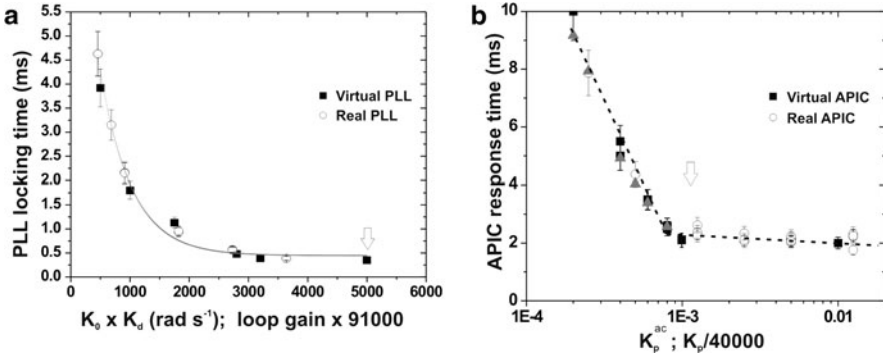
Fig. 5.5 (**a**) Locking time of the simulated (*filled squares*) and real (*empty circles*) PLL vs. loop gains. The arrow indicates the value of the loop gain used experimentally, which corresponds to an optimum behavior of the PLL and a related locking time of about 0.35 ms. The curve is given as a guide to the eye. (**b**) Response time of the APIC vs. K_p^{ac} of the simulated setup and the rescaled K_p gain of the real controller. The two curves match with a reasonable agreement and exhibit two domains: first the response time decreases when increasing K_p^{ac} and then a saturation is reached corresponding to $t_{resp} \simeq 2$ ms. The *dotted line* is given as a guide to the eye. The saturation is due to the contribution of the RMS-to-DC converter (cf. [58] for details)

5.2.3 Main Results

The dynamic performances of each virtual controller have been investigated carefully and compared to those of the real setup. In Fig. 5.5a, b, the locking time of the simulated and real PLL, and the response time of the simulated and real APIC are reported, respectively. Good agreement is obtained between the locking behavior of both PLLs. The optimum locking time of the PLL is found to be about 0.35 ms. The behavior of the amplitude controller is also found to correctly describe the real setup with an optimum response restricted to 2 ms owing to the intrinsic time constant of the RMS-to-DC converter.

5.3 Numerical Implementation of the KPFM Methods: The nc-AFM/KPFM Simulator

Both KPFM operating modes, i.e., Amplitude-Modulation and Frequency-Modulation, AM- and FM-, respectively, have been implemented within the nc-AFM simulator and can be engaged independently. They are implemented as a set of additional building blocks to those of the simulator. The scheme of the numerical implementation of AM- and FM-KPFM methods is reported in Figs. 5.6 and 5.7, respectively.
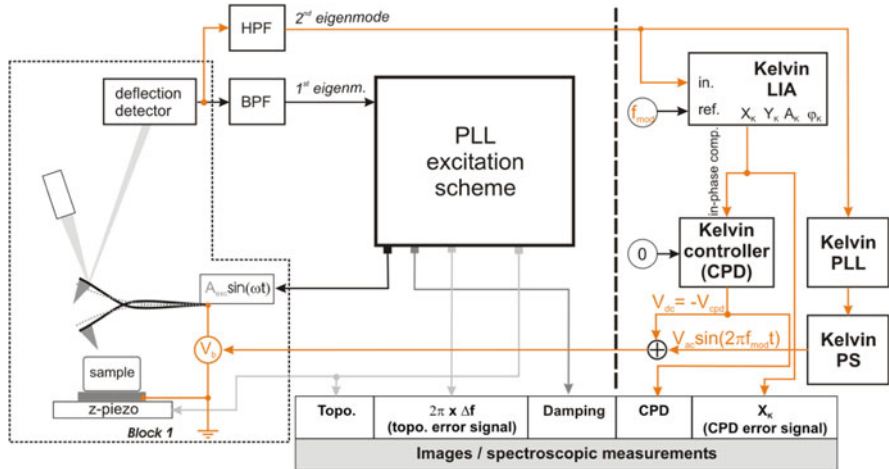
Fig. 5.6 Scheme of the numerical implementation of the AM-KPFM operating mode combined with the nc-AFM simulator
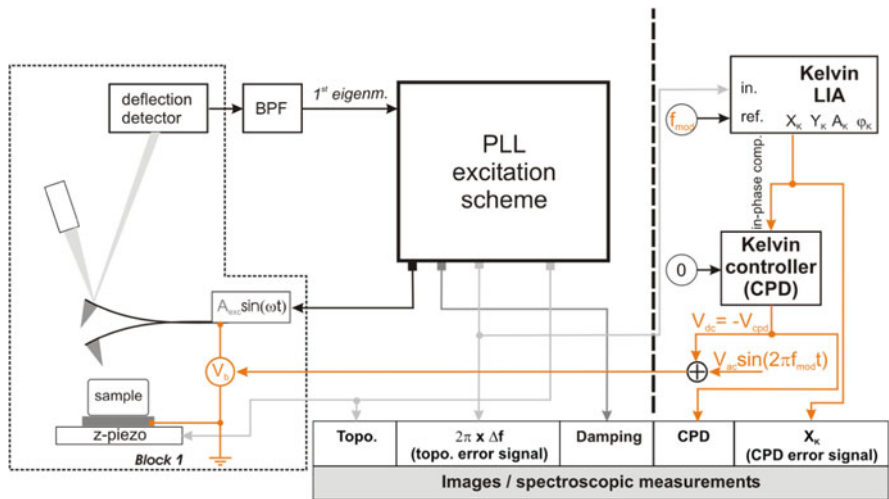

Fig. 5.7 Scheme of the numerical implementation of the FM-KPFM operating mode combined with the nc-AFM simulator

5.3.1 Amplitude-Modulation KPFM (AM-KPFM)

In AM-KPFM, the bias-modulated component is usually the second bending eigenmode of the cantilever, which has been depicted in Fig. 5.6. In this case, the modulation frequency f_{mod} of the applied bias voltage must accurately match the resonance frequency of the mode, f_1 (resonance amplitude A_1). However,

if experiments are to be carried out off-resonance on purpose, i.e., with $f_{mod} \neq f_1$, the numerical implementation will run as well. When using beam-shaped cantilevers, it is known that $f_1 = 6.24 f_0$, which makes f_1 ranging in the MHz regime: $f_1 = 6.24 \times 150\,\text{kHz} \simeq 940\,\text{kHz}$. The instantaneous position of the cantilever connected to that mode, $z_1(t)$, is ruled out by a similar differential equation as the one of the first eigenmode, except that the actuation force (first term on the right-hand side of (5.1)) is now the electrostatic force $F_{es}(V_b, z)$, triggered by the modulation of the applied bias voltage $V_b = V_{dc} + V_{mod} \sin(2\pi f_{mod} t)$:

$$\ddot{z}_1(t) + \frac{\omega_1}{Q_1} \dot{z}_1(t) + \omega_1^2 z_1(t) = \frac{\omega_1^2}{k_1} \left[F_{ext} + F_{int}(z) + F_{es}(V_b, z) \right], \qquad (5.11)$$

where $Q_1, \omega_1 = 2\pi f_1$ and k_1 are the quality factor, resonance angular frequency and effective stiffness of the mode, respectively. F_{ext} stands for the actuation force of the fundamental bending mode of the cantilever. Owing to the large difference between f_0 and f_1, F_{ext} does not influence $z_1(t)$; however, we have kept it in the equation. As already stated, F_{int} stands for all the non-bias-dependent interaction forces. In the above equation, it is important to notice that F_{es} is not only bias dependent, but also z dependent. Hence, the dynamics of the second eigenmode is complex and non-linear, notably in the short-range regime. However, its usually large Q-value in UHV ($Q_1 \simeq 10,000$) combined to the long-range electrostatic interaction allows for the development of the steady state of the eigenmode. Furthermore, although the resonance frequencies of both eigenmodes are far apart, their dynamics are actually coupled by means of the tip-surface separation dependence of the former forces. The instantaneous tip-surface separation $z(t)$ now becomes (cf. Fig. 5.8):

$$z(t) = D - z_0(t) - z_1(t), \qquad (5.12)$$

and consequently $z_\mu = D - A_0 - A_1$.

On the numerical level, although $f_1 \gg f_0$, we have kept the sampling frequency standing for the analog parts of the electronics constant, namely $f_{s_2} = 400\,\text{MHz}$. This is still sufficient to integrate the differential equation with an error kept low enough. The splitting between the first and the second eigenmode is performed using a high-pass filter.[2] A simple first-order high-pass filter has been implemented with the differential equation:

$$\dot{z}_o(t) + \omega_c z_o(t) = \dot{z}_i(t), \qquad (5.13)$$

where ω_c, z_o, and z_i are the cut-off angular frequency, output and input of the filter, respectively. In the code, we have set $\omega_c = 2\pi \times 200\,\text{kHz}$, while f_0 is always $150\,\text{kHz}$ and hence, $f_1 = 940\,\text{kHz}$.

---

[2]On the experimental level, the AM-KPFM setup requires that the bandwidths of the PSD and of the preamplifier are large enough to allow for the detection of the 2nd eigenmode without attenuation.
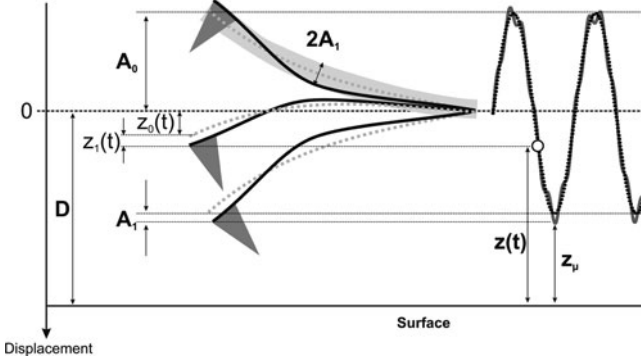
Fig. 5.8 Definition of the geometrical parameters used for the description of the combined vibrations of the fundamental and second eigenmodes of the cantilever in AM-KPFM. The time-dependent vibration is shown on the right-hand side of the figure

The Kelvin LIA detects the vibration amplitude of the second bending eigenmode of the cantilever with a 10 kHz bandwidth. The LIA provides $A_K = 2\sqrt{X_K^2 + Y_K^2}$, which in the case of the AM-KPFM matches A_1. The Kelvin controller has a 2.5 kHz bandwidth. It is a standard proportional and integral controller, the numerical implementation of which is similar to the distance and amplitude controllers of the PLL-excitation scheme. It provides the DC part of the bias that minimizes, or ideally nullifies, the vibration amplitude of the second eigenmode and hereby compensates the CPD. When the tip is biased (sample grounded), $V_{dc} = -V_{CPD}$, otherwise $V_{dc} = +V_{CPD}$. It is important to notice that the input of the controller is not the signal detected by the Kelvin LIA, A_K, but the in-phase component X_K. The in-phase component is supposed to be used instead of A_K because it can become negative and thus handle negative error signals, while A_K cannot.

The code integrates (5.11) in parallel to the equation of motion for the fundamental flexural eigenmode. The PLL-excitation scheme ensures that the latter mode is continuously actuated at its resonance frequency that shifts as the tip is approached to the surface. Meantime, the second mode undergoes a frequency shift as well. Nevertheless, it is mandatory to maintain the on-resonance excitation for this eigenmode too; otherwise, the vibration amplitude A_K does not match the resonance value, A_1. Experimentally, this requires one to tune precisely the modulation frequency of the bias f_{mod} to recover the on-resonance excitation *as soon as the tip is approached to the surface* and prior to engaging the Kelvin controller and scanning. Performing this step numerically is time consuming as the frequency sweep has to be performed slowly owing to the large value of Q_1. In order to avoid that, an additional PLL, the Kelvin PLL, has been implemented with the goal to continuously track the shift of f_1 while approaching the surface, i.e., as a function of the tip-surface separation. Thus, the AC part of the bias modulation always matches the interaction-shifted resonance frequency of the second eigenmode $\widetilde{f}_{mod}$: $V_{mod} \sin(2\pi \widetilde{f}_{mod} t + \varphi_K)$, φ_K being the phase shift introduced by the Kelvin PLL while processing the input signal. The

numerical implementation of the Kelvin PLL is strictly similar to the one used in the PLL-excitation scheme for the fundamental eigenmode. Then, after a proper phase shifting process, which is insured by the Kelvin phase shifter, the modulation signal $V_{mod} \sin(2\pi \widetilde{f}_{mod} t)$ is supplied to the cantilever and hence, the on-resonance condition is maintained. Furthermore, the frequency of the reference signal for the Kelvin LIA, f_{mod}, is continuously updated, which makes the detection of A_1 continuously self-consistent. As said before, this step merely concerns the approach of the tip to the surface. As soon as the required Δf is reached, i.e., prior to engaging the Kelvin controller and scanning or recording a spectroscopic curve, the Kelvin PLL is disengaged and the modulation then continuously performed at the last computed value of $\widetilde{f}_{mod}$.

5.3.1.1 Maximization of the In-Phase Component of the Kelvin LIA

On the experimental level, in addition to the above comment on the adjustment of $\widetilde{f}_{mod}$, the phase of the Kelvin LIA is to be adjusted to get always a maximal in-phase signal and hence optimize the measurement of the bias-modulated vibration amplitude. This is an irrelevant issue for the simulator as there is no additional "numerical" phase delay between the LIA and the bias modulation. The phase of the LIA is always exactly the same as the one of the in-phase component. Hence, the in-phase signal is always maximum.

5.3.2 Frequency Modulation KPFM (FM-KPFM)

Unlike in AM-KPFM, the FM-KPFM method does not rely on the detection of a mechanical resonance of the cantilever, but on the detection of the bias-induced modulation of the frequency shift of the fundamental eigenmode of the cantilever. However in this case, the numerical implementation is made easier as no Kelvin PLL is required. The numerical scheme is reported in Fig. 5.7. In FM-KPFM, the modulation frequency of the bias is performed at low frequency, typically $f_{mod} = 1$ kHz. In order to understand how the bias modulation induces the modulation of the Δf, let us consider the following elements. To first order, it is known that the interaction-shifted resonance frequency $\widetilde{f}_0$ of the fundamental bending eigenmode of the cantilever under the influence of an interacting force with the general form $F_{int}(z)$ may be written as:

$$\widetilde{f}_0 = \frac{1}{2\pi} \sqrt{\frac{k_0 - \partial F_{int}/\partial z}{m_0}} = f_0 \left(1 - \frac{1}{2k_0} \frac{\partial F_{int}}{\partial z}\right) \iff \Delta f = \widetilde{f}_0 - f_0 = -\frac{1}{2k_0} \frac{\partial F_{int}}{\partial z}.$$
(5.14)

If one assumes that the interaction force includes an electrostatic component with the usual capacitive form: $F_{int}(z) \propto F_{es}(V_b, z) = 1/2 \partial C/\partial z V_b^2$ with $V_b = V_{dc} - V_{cpd} + V_{mod} \sin(2\pi f_{mod} t)$, then it can readily be seen that a modulation at f_{mod} and $2f_{mod}$ will occur in the force and hence, in the frequency shift (5.14). The

DC bias voltage nullifying the modulated component of the Δf at f_{mod} gives the CPD. In other words, in FM-KPFM, the amplitude of the bias-induced modulation of the Δf has the same role as the bias-induced resonance of the second eigenmode of the cantilever (resonance amplitude A_1) in AM-KPFM. The underlying idea of the FM-KPFM method is that it is not sensitive to the electrostatic force like in AM-KPFM (A_1 being proportional to the strength of F_{es}), but rather to its gradient (readily visible in (5.14)). Owing to the lower modulation frequency, the Kelvin LIA has a lower, 500 Hz, bandwidth.

5.3.3 Methodology with the nc-AFM/KPFM Simulator

The sequence of simulation of a spectroscopic curve or an image in FM- or AM-KPFM is detailed in Fig. 5.9. It follows accurately the experimental protocols and is cast into three main steps:

1. The steady state of the cantilever is calculated for a tip-surface separation corresponding to twice the vibration amplitude of the first bending mode of the cantilever (typically 8 nm peak-to-peak). Then (1) the PLL is engaged, (2) the phase lag of the phase shifter is adjusted to maximize the oscillation amplitude (on-resonance condition), (3) the APIC is engaged, and (4) the bias modulation is engaged (i.e., $f_{mod} \neq 0$ and $V_{mod} \neq 0$) to trigger the long-range electrostatic force (see (5.5)). Note that if the AM-KPFM is engaged, the Kelvin PLL must be engaged as well. At this point, the cantilever is operated in nc-AFM and the surface may be approached. At this distance, this should yield an almost zero long-range interaction if the tip would carry no charge. However, in the atomistic description of the tip as described in the next section (Sect. 5.4), the tip carries an intrinsic charge of $+1$ that induces a long-range electrostatic background force. Thus, a DC voltage, $V_{dc}^{ref} = -0.91$ V, is applied to the tip to compensate for it and nullify the LCPD at large tip–sample separation (>2 nm). V_{dc}^{ref} can be interpreted as the opposite of the macroscopic CPD of the electrodes-bulk NaCl system. Thus, the bias voltage applied to the tip is $V_b = V_{dc} + V_{dc}^{ref} + V_{mod} \sin(2\pi f_{mod}t)$. Then the approach is engaged down to an arbitrary value of tip-surface separation.
2. The Kelvin controller and the distance controller are engaged sequentially. Impulse response tests are then performed with the amplitude controller and the distance controller to assess their time constant and make sure that they are in a critically damped regime. It is important to perform these tests when the tip is close to the surface. Then, imaging artifacts that would be due to an inadequate choice of the gains of the controllers are unlikely to occur.
3. The spectroscopic curve (i.e., Δf vs. V_{dc} in FM-KPFM, or A_1 vs. V_{dc} in AM-KPFM) or the scan is engaged. Note that if operating in AM-KPFM, the Kelvin PLL is disengaged first and $\widetilde{f}_{mod}$ kept constant and equal to the latest value computed during the approach, as stated before. If a spectroscopic curve is to be performed, then the Kelvin controller and the distance controller are disengaged
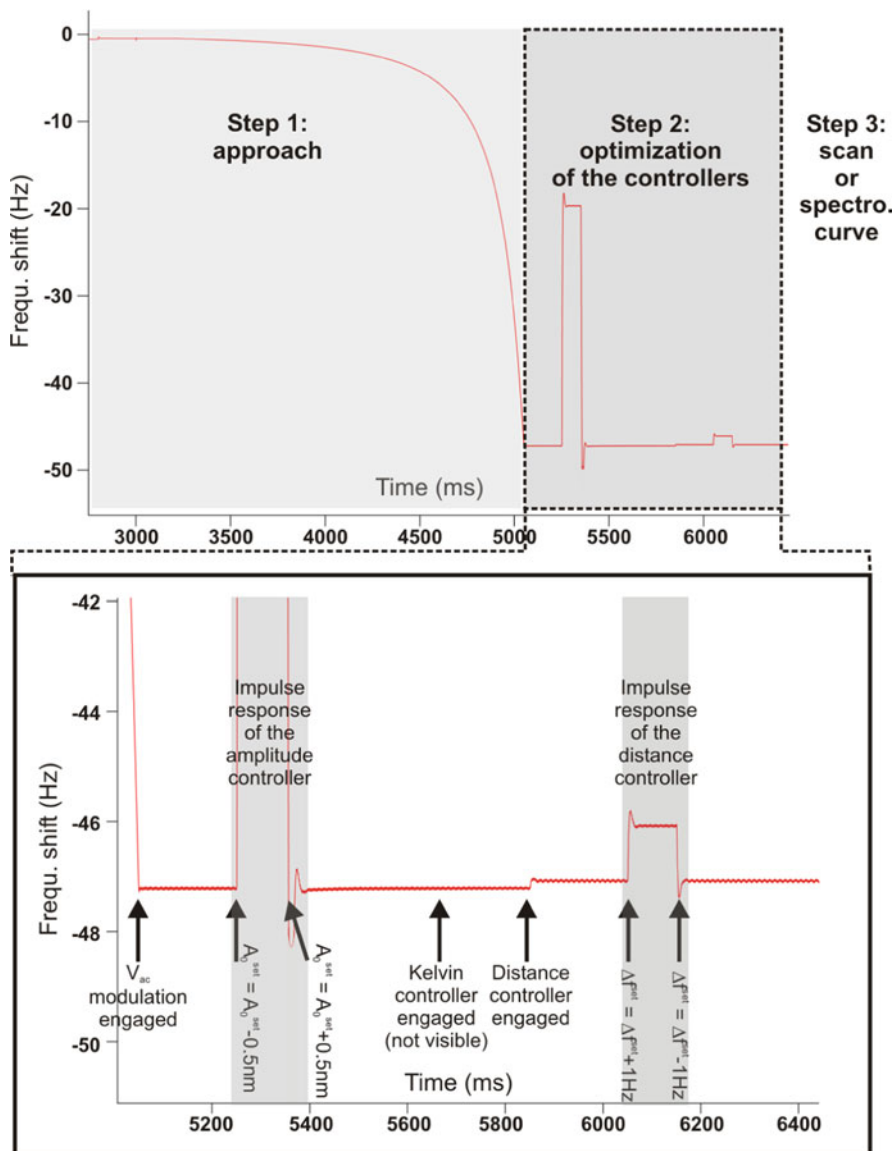
Fig. 5.9 Sequence of simulation of a spectroscopic curve or an image with the nc-AFM/KPFM simulator. When the tip is approached to the surface, the time constant of the controllers is carefully adjusted to make sure that they do not influence the subsequent measurements

(AM- or FM-KPFM). The AC modulation may remain engaged or not. The spectroscopic curve is acquired by continuously sweeping the DC part of the bias, first from 0 down to negative values and then upward. For that purpose, we use a sweep speed of about $200\,\mathrm{mV\,s^{-1}}$, which is slow enough to prevent nonadiabatic effects from occurring.

5.4 Atomistic Simulations of Bias Voltage-Dependent Force Fields

The two following sections report the results obtained when combining the nc-AFM/KPFM simulator and atomistic calculations of the bias voltage and distance-dependent interaction force field computed between a metallic tip carrying an ionic cluster and the (001) facet of a NaCl crystal, as sketched in Fig. 5.10a. For that work, the nc-AFM/KPFM has been used in the FM-KPFM mode. Most of the elements detailed below are reported in [36]. We first give the expression of the Madelung surface potential for the ionic crystal and then describe the atomistic simulations of the tip-surface interaction. Finally, the results of the calculations performed with the nc-AFM/KPFM simulator are given.

5.4.1 Madelung Surface Potential of an Alkali Halide

In order to assess how quantitative the KPFM measurements on the atomic-scale can be, it is important to estimate the physical observable to which the LCPD might be connected to, namely the Madelung surface potential V_s of the alkali halide crystal. V_s can be estimated on the base of the work by Watson et al. [68] and may be written in the form [19]:

$$V_s(x, y, z_\mu) = -\frac{q}{\pi\epsilon_0 a'} \cosh\left[\frac{2\pi}{a'}\delta^\perp(V_b)\right] \widetilde{\chi}(x, y)e^{-\frac{2\pi}{a'}z_\mu} \qquad (5.15)$$
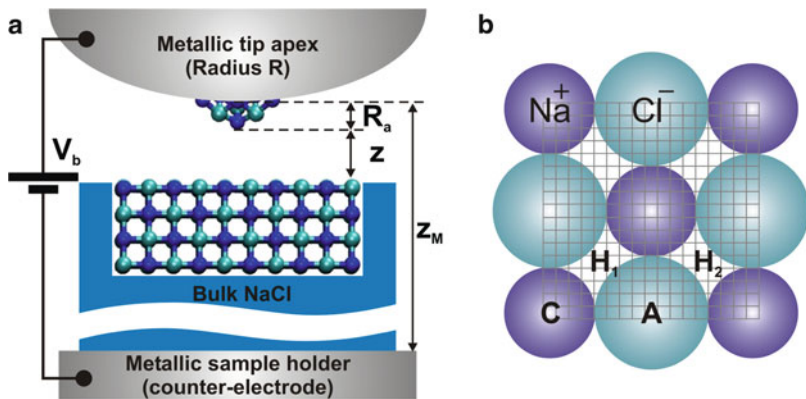

Fig. 5.10 (**a**) Sketch of the numerical tip-surface setup. We have set $z_m = 5$ mm compared to z which scales in the sub-nm range. (**b**) Sketch of the NaCl unit cell showing the 17×17 mesh used to calculate the (x, y, z, V) four-dimensional tip-surface force field. Four particular sites have been investigated: anionic (A), cationic (C), and hollow (H_1, H_2) sites
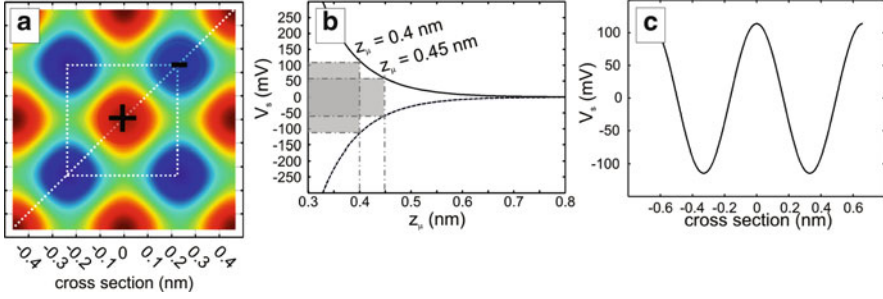
Fig. 5.11 (**a**) Madelung surface potential calculated from (5.15) for $z_\mu = 4$ Å. The vertical contrast ranges from -100 (*blue spots*) to $+100$ mV (*red spots*). The *dotted square* stands for the unit cell shown in Fig. 5.10b, i.e., centered on top of a cation. (**b**) Distance dependence of the potential on top of an anion (*dotted curve*) and on top of a cation (*solid curve*) showing the exponential decay of the potential. At $z_\mu = 0.4$ nm, the total magnitude of the potential is $\simeq 220$ mV and becomes $\simeq 140$ mV for $z_\mu = 0.45$ nm. (**c**) Cross section along the dotted diagonal line shown in (**a**)

with: $\widetilde{\chi}(x, y) = \cos\left[\frac{2\pi}{a'}(x - x_0)\right] + \cos\left[\frac{2\pi}{a'}(y - y_0)\right]$, a spatial modulation term. x_0 and y_0 are the x and y coordinates of the center of the asperity projected onto the unit cell. Setting $x_0 = y_0 = 0$ locates the asperity and therefore the tip on top of an anion. a' is a geometrical parameter connected to the lattice constant of the crystal, a, according to: $a' = a\sqrt{(2)/2}$. $\delta^\perp(V_b)$ depicts the vertical displacement (i.e., in the perpendicular direction compared to the plane of the crystal) of the ion owing to its ionic polarizability. z_μ depicts the distance from the plane of the crystal above which the surface potential is estimated. z_μ will state for the distance between the lowest turning point of the tip oscillation cycle and the surface, as stated before. The above expression exhibits the expected exponential decaying behavior as a function of z_μ. The potential is reported in Fig. 5.11 for $a = 0.66$ nm, $\delta^\perp = 11$ pm and $z_\mu = 4$ Å [19].

5.4.2 Atomistic Simulations of the Bias Voltage-Dependent Force Field

The calculations of the force field were performed using atomistic simulations as implemented in the code SCIFI [38]. The interatomic forces are computed from a sum of pairwise Buckingham potentials acting between ions. These are treated atomistically in a shell model with coupled oppositely charged cores and shells in order to describe their polarizabilities. The SCIFI code also allows for the inclusion of metallic electrodes at the tip and below the surface. The interaction of these with ions in the surface and tip are treated by the method of images [38]. Using this approach, we can simulate the polarization of conductors and resultant atomic geometries in the system as a function of tip position and applied bias voltage.

Parameters for the species considered were taken from [69]. All cores and shells were allowed to relax completely with respect to interatomic and image forces with a convergence criterion of 1 meV/Å per ion, the magnitude of the force difference with voltage and distance being of the order of several tenths of an eV/Å. Hence, in the present simulations we take into account ionic relaxation, and electronic and ionic polarization as a function of both atomic interactions and applied bias.

The properties of the NaCl(001) surface are well understood and can be well represented by a slab of four atomic layers containing 10×10 ions, with those in the bottom layer and edges kept fixed (cf. Fig. 5.10a). The NaCl slab is embedded within a semi-infinite, 5 mm thick, slab merely treated by means of its dielectric constant. For the tip, a 64-atom cubic cluster of NaCl is embedded into a metallic sphere of radius $R = 5$ nm and oriented such that the [111] direction is perpendicular to the surface with a Na atom at the apex. The main condition for finding a suitable tip beyond comparing to experimental contrast is the stability of the tip-surface system. Here, we refer to the onset of tip and surface atom instabilities, i.e., large irreversible displacements that would either cause a tip crash in experiments or directly introduce numerical instabilities due to the difficulty in finding the equilibrium geometry. We considered many tip models, and the most stable configuration of the tip is found when the cluster protrudes from the end of the sphere with a height $R_a = 0.3$ nm (cf. Fig. 5.10a). This tip carries an intrinsic charge of $+1$ due to its stoichiometry, inducing an opposite charge in the vicinity of the metallic part of the tip. The NaCl atoms within the sphere are frozen and play no role in the calculation of image forces. They act as ghost metal atoms stabilizing the tip apex. The metallic part of the tip is biased with respect to the counter-electrode holding the crystal.

In order to compute images with the simulator, the NaCl unit cell was meshed with a 17×17 grid (cf. Fig. 5.10b). For each pixel of the mesh, the distance dependence (z-dependence) of the atomistic force field is computed by 10 pm steps from 0.3 to 2.0 nm (171 samples) and the bias dependence (V-dependence) by 100 mV steps from -3.4 to $+2.3$ V (57 samples). It must be noticed that each (z, V) couple of coordinates provides not only the value of the force, but also the position of the core and of the shell of each ion of the setup (464 in total). This results in a very large amount of data to store and handle, about 600 GB uncompressed. The simulation runs are farmed onto a cluster of several hundred workstations, with each grid point and voltage combination run on a single core for every tip height. On Intel 2.5 GHz processors or equivalent, this takes about an hour and calculating the full map takes about 16,000 h of CPU time. Post-processing of the data takes a similar amount of time.

To make the simulations with the nc-AFM/KPFM simulator more accurate and reduce the numerical noise further, the atomistic force field is post-processed as follows. For each pixel of the mesh, the (z, V) force matrix that is built from the raw data is z- and V- interpolated with a Cubic Spline function by 5 pm and 10 mV steps, respectively. In addition to the short-range atomistic force field, the long-range interaction including Van der Waals and electrostatic contributions as described in

Sect. 5.2 is added and the cut-off distance setting the size of the lookup table is set arbitrarily to 8 nm. Above 8 nm, the van der Waals and electrostatic long-range contributions are not set to 0, but estimated out of their analytical expressions, (5.4) and (5.5), respectively. Therefore, the total 4-dimensional lookup table of the force field to be used with the simulator consists of $x \times y \times z \times V = 17 \times 17 \times (8\,\text{nm}-0.3\,\text{nm})/0.005\,\text{nm} \times (2.3\,\text{V}-(-3.4\,\text{V}))/0.01\,\text{V} \simeq 255 \cdot 10^6$ samples, which requires 8 GB of RAM on the host computer (Intel Core2Duo, 2.5GHz/proc.). With the parameters detailed above, approaching the tip to the surface typically takes 5 min. Computing a spectroscopic curve takes about 30 min and computing an image about 2 h. The spectroscopic curves shown below have been computed on top of four particular sites of the mesh: an anionic site A, a cationic site C, and the two hollow sites H_1 and H_2, which are made inequivalent owing to the orientation of the cluster with respect to the surface symmetry.

Force vs. distance curves computed above the four sites with $V_{dc} = 0\,\text{V}$ are shown in Fig. 5.12a. Below 0.45 nm, tip/surface instabilities on top of anionic and hollow sites occur. Above 0.45 nm, the curves differ significantly, although exhibiting similar features to those reported with almost equivalent setups [20, 22, 70]. Force vs. V_{dc} curves measured at $z_\mu = 0.45\,\text{nm}$ are shown in Fig. 5.12b for the four sites. The maxima of the curves differ between sites (cf. dotted lines): $-304\,\text{pN}$ at 1.22 V (site C) and $-506\,\text{pN}$ at 1.06 V (site A). The curves systematically deviate from the capacitive, parabolic-like, behavior which stems from the polarization of the ions at the tip–surface interface. To assess this, the displacements of the cores of the foremost Na^+ ion of the tip (δ_{Na}^T) when placed above a Na^+ (δ_{Na}^S) and above a Cl^- (δ_{Cl}^S) of the slab as a function of V_{dc} are shown in Fig. 5.12c, d, respectively. They are measured at $z_\mu = 0.45\,\text{nm}$. A positive displacement means that the ion is displaced upward (e.g., toward the tip when considering an ion of the slab). We only have focused on the displacements of the cores of the ions that were judged as the most significant, although the polarization process involves all the ions of the interface and their shells. For the sake of clarity, we have also sketched the ionic displacements in Fig. 5.12e, f.

The calculations show that on top of Na^+ at zero bias, the foremost cation of the tip is attracted toward the surface: $\delta_{Na}^T = -8.5\,\text{pm}$. Simultaneously, the Na^+ of the slab undergoes a moderate displacement toward the tip: $\delta_{Na}^S = +2\,\text{pm}$. This behavior stems from the balance between the short-range chemical interaction and the local electrostatic interaction due to the intrinsic charge of the tip, merely compensated by V_{dc}^{ref} at large distance. With $V_{dc} > 0$, the foremost cation of the tip remains attracted to the surface, while the Na^+ is repelled within the slab. The short-range electrostatic force is then strengthened between the tip cation and the four Cl^- closest neighbors of the Na^+ of the slab, while the latter is repelled from the tip because of the overall less favorable chemical and electrostatic interaction. With $V_{dc} < 0$, the electrostatic force becomes dominant and mostly repulsive for the same reason as before. Then the set of Cl^- and Na^+ ions are repelled within the slab.

On top of Cl^- at zero bias, the favorable combination between the chemical interaction and the local electrostatic interaction due to the intrinsic charge of the tip partly compensated by V_{dc}^{ref} produces significant displacements of the ions at
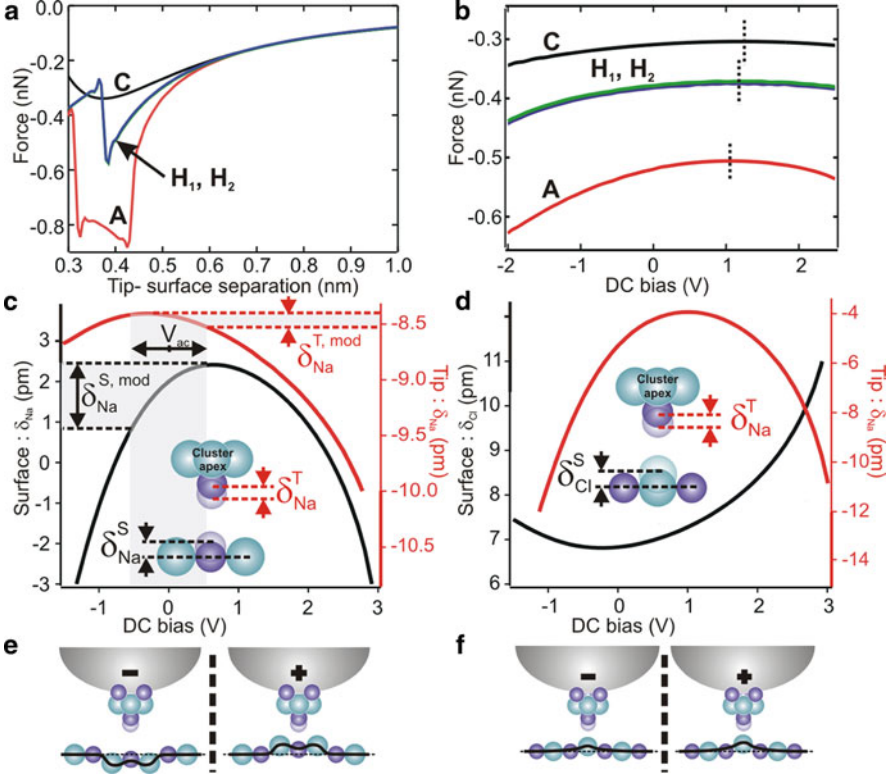
Fig. 5.12 (**a**) Force vs. distance curves measured above the four sites of the unit cell at $V_{dc} = 0\,V$. Below 0.45 nm, the tip becomes unstable. (**b**) Force vs. V_{dc} curves at $z_\mu = 0.45\,nm$. The dependence is not parabolic. (**c**) V_{dc} dependence of the displacement of the foremost Na^+ ion of the tip, δ^T_{Na}, at $z_\mu = 0.45\,nm$ on top of Na^+ of the slab and corresponding δ^S_{Na} displacement. The AC bias modulation (*gray*) triggers the dynamic displacement of the ions at the interface ($\delta^{T,S,mod}_{Na}$). (**d**) Same as c- except that the tip is now placed on top of Cl^-. (**e**) Scheme of the ionic displacements induced by the tip on top of Na^+ as a function of the sign of the bias voltage. (**f**) Same as (**e**) except that the tip is now on top of Cl^-

the interface ($\delta^T_{Na} = -6\,pm$; $\delta^S_{Cl} = +7\,pm$). With $V_{dc} > 0$, the local electrostatic interaction increases the mutual attraction between ions. With $V_{dc} < 0$, the Cl^- of the slab is less attracted by the tip due to the repulsive electrostatic interaction, but the tip cation remains attracted by the surface, likely because the chemical interaction is still large enough.

These conclusions stress that, when the KPFM controller is engaged, the AC modulation of the bias triggers complex dynamic displacements of the cluster/surface ions. As predicted in [19], these displacements support the LCPD signal and explain the deviation from the usual capacitive parabolic law of the force vs. bias voltage curve. Indeed, when performing the following simulations while freezing the ionic polarization, no KPFM contrast occurs (data not shown).

5.5 Results with the nc-AFM/KPFM Simulator

The main parameters for the simulations shown in this section are: oscillation amplitude: 8 nm peak-to-peak, cantilever resonance frequency: 150 kHz, cantilever stiffness: $30\,\mathrm{N\,m^{-1}}$, Q-factor: 30,000, scan size: $1.03 \times 1.03\,\mathrm{nm^2}$, scan speed: 1.5 s/line. The FM-KPFM mode was implemented with a 500 Hz bandwidth lock-in amplifier and a 50 Hz bandwidth controller. The AC bias modulation is $V_{\mathrm{mod}} = 0.5\,\mathrm{V}$ and $f_{\mathrm{mod}} = 1\,\mathrm{kHz}$.

5.5.1 Spectroscopic Curves

The distance dependence of the LCPD has first been investigated by means of spectroscopic curves. When the tip is biased, the maximum of the Δf vs. V_{dc} curve gives a DC voltage opposite to that of the LCPD: $V_{\mathrm{dc}} = -V_{\mathrm{LCPD}}$. In Fig. 5.13a, spectroscopic curves measured on top of each site for a tip-surface separation $z_{\mu} = 0.45\,\mathrm{nm}$ are shown. As expected from the force vs. V_{dc} curves, the spectroscopic curves deviate from the parabolic-like behavior (shown for site A, dotted gray curve) and the positions of the maxima differ upon sites. Furthermore, the latter positions do not match those of the force vs. V_{dc} curves. However, such an effect is expected to occur as soon as the z and V dependencies of the interaction force cannot be separated, i.e., $F(z, V_{\mathrm{dc}}) \neq h(z)g(V_{\mathrm{dc}})$.[3] A shift of +0.87 V is measured from site A to site C, consistently with the larger repulsive electrostatic force observed above cations. These measurements have been reproduced for various tip-surface separations and gathered in Fig. 5.13b. When increasing the separation, the LCPD first decreases and then increases to converge toward 0 at large distance, as stated before. Below 0.6 nm, the curves unbundle and differ significantly upon sites (gray area). These curves are equivalent to Δf vs. distance curves that are driving the magnitude of the topography contrast. Hence, a site-dependent KPFM contrast is indeed expected while scanning for tip-surface separations smaller than 0.6 nm.

---

[3]The expressions of the DC value of the bias voltage that maximizes $\Delta f(z, V_{\mathrm{b}})$ and the force $F(z, V_{\mathrm{b}})$ with $V_{\mathrm{mod}} = 0$, i.e., within the framework of spectroscopic curves in FM- and AM-KPFM, respectively are given by: $(\partial \Delta f(z, V_{\mathrm{b}})/\partial V_{\mathrm{dc}})|_{V_{\mathrm{mod}}=0} = 0(1)$ and $(\partial F(z, V_{\mathrm{b}})/\partial V_{\mathrm{dc}})|_{V_{\mathrm{mod}}=0} = 0(2)$, respectively. The expression of Δf is derived from the approach by Giessibl [71]: $\Delta f(z, V_{\mathrm{b}}) \propto \int_0^{T_0} F(z, V_{\mathrm{b}}) \sin(\omega_0 t)\mathrm{d}t$ with: $V_b = V_{\mathrm{dc}} - V_{\mathrm{CPD}} + V_{\mathrm{mod}} \sin(\omega_{\mathrm{mod}}t)$. If the force has the usual quadratic-like form: $F(z, V_{\mathrm{b}}) = h(z) \times V_{\mathrm{b}}^2$ (e.g., $F = \frac{1}{2}\partial C/\partial z V_{\mathrm{b}}^2$), then conditions (1) and (2) yield equivalently to $V_{\mathrm{dc}} = V_{\mathrm{CPD}}$. However, if the force has a less usual fully polynomial form, as this is the case when dealing with SRE forces [19,36]: $F(z, V_{\mathrm{b}}) = h(z) \times [A(z)V_{\mathrm{b}}^2 + B(z)V_{\mathrm{b}} + C(z)]$, then conditions (1) and (2) give: $V_{\mathrm{dc}} = V_{\mathrm{CPD}} - I'/(2J')$ (with $I' = \int_0^{T_0} B(z)h(z) \sin(\omega_0 t)\mathrm{d}t$ and $J' = \int_0^{T_0} A(z)h(z) \sin(\omega_0 t)\mathrm{d}t$) and $V_{\mathrm{dc}} = V_{\mathrm{CPD}} - B(z)/(2A(z))$, respectively. Therefore the maxima of both spectroscopic methods differ. The main reason is that the force is dynamically z-dependent (which makes the compensated CPD z-dependent as well, as seen with the above equation), while Δf is averaged over the oscillation cycle, hereby averaging the force as well.
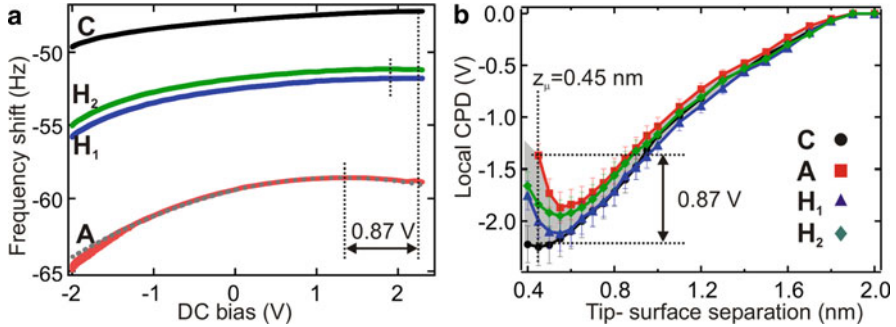
Fig. 5.13 (**a**) Spectroscopic curves computed above the four sites at $z = 0.45$ nm. A shift of 0.87 V is noticed between anionic (A) and cationic (C) sites. (**b**) Distance dependence of the LCPD above the four sites derived from the spectroscopic curves. In the short-range regime, the LCPD exhibits a resonance-like and site-dependent behavior

The magnitude of the LCPD contrast can be derived as well. At $z = 0.45$ nm (dotted line), a maximum of 0.87 V is expected. At equivalent height, the Madelung surface potential is 0.14 V (cf. Fig. 5.11b). This resonance-like effect has been predicted theoretically [36] and reported experimentally [27]. It relies on a subtle balance between short-range and long-range electrostatic forces, both weighting in the manner the LCPD is compensated.

5.5.2 Topography and LCPD Images

Finally, topography and LCPD images have been computed (cf. Fig. 5.14a–c, respectively). Images shown in Figs. 5.14a (38 pm full scale) and 5.14b (0.56 V full scale) have been simultaneously computed with the distance controller engaged. The scan has been engaged on top of a cation at $z_\mu = 0.45$ nm, corresponding to $\Delta f_{\text{set}} = -47.22$ Hz. The dotted area depicts the unit cell shown in Fig. 5.10b. Topography and LCPD images show cations as depressions, consistently with spectroscopic curves. The magnitude of the contrasts as well as the distance range are in good agreement with our former experimental observations (30 pm, 0.1 V) [19]. Figure 5.14c (0.86 V full scale) is an LCPD image computed with similar conditions as (b), but at constant height $z = 0.45$ nm, i.e., with the distance controller disengaged. The magnitude of the contrast matches the predicted behavior (cf. Fig. 5.13b, dotted line). In Fig. 5.14d is reported the magnitude of the LCPD contrast as a function of the tip-surface separation (left-hand side). The curve is deduced from scans for which the distance regulator was engaged. The average value of the LCPD (mean contrast) has been reported as well (right-hand side). It follows accurately the evolution of the average LCPD derived from the spectroscopic curves (cf. Fig. 5.13b). The contrast expands around the average value while keeping confined within the gray area, the size of which is controlled by the
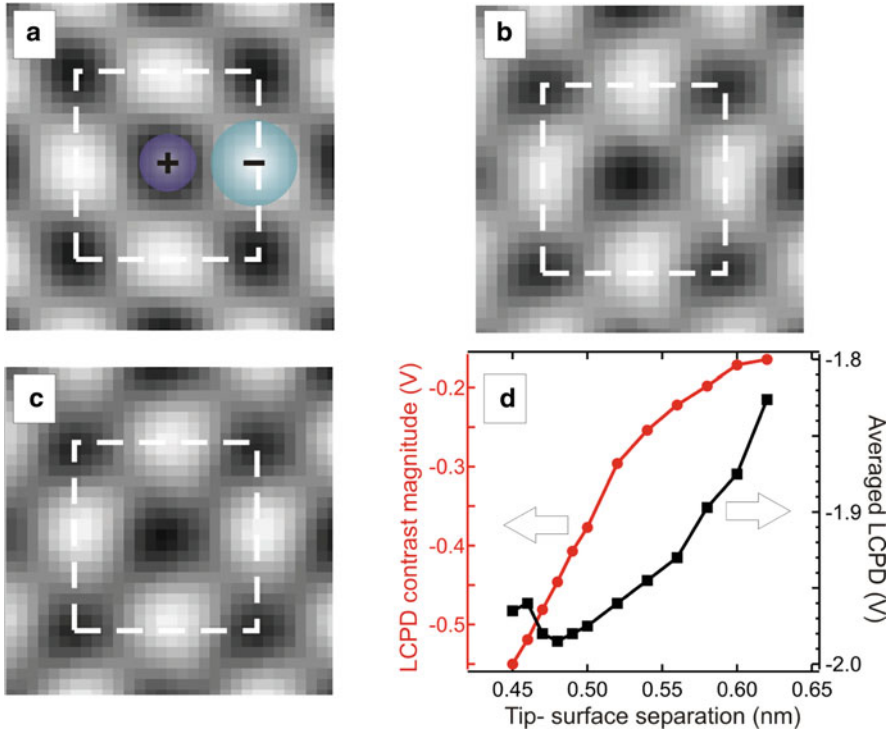
Fig. 5.14 (**a**) Topography image computed with the nc-AFM/KPFM simulator. The vertical contrast is 38 pm. (**b**) Simultaneously computed LCPD image. The contrast ranges from -2.24 to -1.69 V (0.56 V full scale). In both channels, cations are imaged as depressions and anions as protrusions. (**c**) LCPD image computed at constant height, $z_\mu = 0.45$ nm. The contrast ranges from -2.24 to -1.38 V (0.86 V full scale), consistently with the expected range deduced from Fig. 5.13b. (**d**) Evolution of the magnitude of the LCPD contrast (*dots*) and of the mean LCPD (*squares*) as a function of the distance

combination between short-range electrostatic and chemical forces. We infer from the above elements that relevant information about the LCPD is not only carried by the magnitude of the KPFM contrast, but also by its average value.

5.6   Conclusions and Outlook

The focus of this chapter was to present recent numerical developments targeted at helping the interpretation of the atomic-scale contrast in KPFM, which inherently requires (1) an accurate atomistic description of the force field occurring between the tip and the surface, and (2) a proper numerical implementation of the control electronics of the nc-AFM/KPFM setup. In the case of the bulk ionic crystal discussed here, it has been shown that short-range electrostatic forces occur in the

range of 4–6 Å above the surface and differ between cationic and anionic sites. When combined with the chemical short-range forces, these are responsible for the simultaneous topographical and CPD atomic-scale contrast. However, SRE forces are self-consistently correlated with the chemical forces as the modulated bias voltage triggers ionic displacements at the tip–surface interface. Therefore, because the occurrence of the atomic-scale KPFM contrast relies on the latter displacements, the magnitude of the LCPD differs from the Madelung surface potential at equivalent height, *although the spatial periodicity of both observables remains the same, i.e., the one of the ionic lattice*. Thus, the quantitative interpretation of the atomic-scale CPD contrast must be done within the context of SRE forces and not in terms of physical observables such as the Madelung surface potential or the local work function. This is all the more true in that the effects are strongly dependent of the tip shape and size, which has also been reported experimentally (cf. footnote ♯29 in [72]).

An important part of the problem that was not addressed here is the contribution of long-range electrostatic interactions to the observed LCPD. The influence of these on the magnitude of the KPFM contrast has not yet been investigated in detail on the numerical level, despite that the effects are theoretically predicted [36]. Another issue deals with the use of KPFM on the atomic scale to map the chemical identity of atoms. The underlying idea is to assess how sensitive the atomic-scale CPD contrast is to the tip termination and intrinsic charge. If the CPD contrast remains qualitatively unchanged from one tip to the other (e.g., cations=dark contrast, anions=bright contrast, as shown here), then the KPFM channel could unravel in a straightforward and univocal manner the delicate issue of chemical identification, which usually requires a thorough analysis. The two latter issues are currently being addressed. "There's plenty of room at the bottom", R. Feynman, meeting at Caltech on December 29, 1959.

References

1. A. Kikukawa, S. Hosaka, R. Imura, Rev. Sci. Instrum. **67**(4), 1463 (1996)
2. S. Kitamura, M. Iwatsuki, Appl. Phys. Lett. **72**, 3154 (1998)
3. S. Sadewasser, M. Lux-Steiner, Phys. Rev. Lett. **91**, 266101 (2003)
4. S. Sadewasser, T. Glatzel, R. Shickler, Y. Rosenwaks, M. Lux-Steiner, Appl. Surf. Sci. **210**((1–2)), 32 (2003)
5. S. Sadewasser, P. Carl, T. Glatzel, M.C. Lux-Steiner, Nanotechnology **15**, S14 (2004)
6. J. Polesel-Maris, A. Piednoir, T. Zambelli, X. Bouju, S. Gauthier, Nanotechnology **15**, S24 (2004)

7. C. Sommerhalter, T. Matthes, T. Glatzel, A. Jäger-Waldau, M.C. Lux-Steiner, Appl. Phys. Lett. **75**, 286 (1999)
8. Y. Rosenwaks, R. Shikler, T. Glatzel, S. Sadewasser, Phys. Rev. B **70**, 085320 (2004)
9. H. Hoppe, T. Glatzel, M. Niggemann, A. Hinsch, M.C. Lux-Steiner, N.S. Sariciftci, Nanoletters **5**, 269 (2004)
10. S. Kitamura, K. Suzuki, M. Iwatsuki, Appl. Surf. Sci. **140**, 265 (1999)
11. Y. Sugawara, T. Uchihashi, M. Abe, S. Morita, Appl. Surf. Sci. **140**, 371 (1999)
12. S. Kitamura, K. Suzuki, M. Iwatsuki, C. Mooney, Appl. Surf. Sci. **157**, 222 (2000)
13. K. Okamoto, K. Yoshimoto, Y. Sugawara, S. Morita, Appl. Surf. Sci. **210**, 128 (2003)
14. K. Okamoto, Y. Sugawara, S. Morita, Jpn. J. Appl. Phys. **42**, 7163 (2003)
15. T. Arai, M. Tomitori, Phys. Rev. Lett. **93**, 256101 (2004)
16. F. Krok, K. Sajewicz, J. Konior, M. Goryl, P. Piatkowski, M. Szymonski, Phys. Rev. B **77**(23), 235427 (2008)
17. A. Sasahara, C.L. Pang, H. Onishi, J. Phys. Chem. B **110**, 13453 (2006)
18. G. Enevoldsen, T. Glatzel, M. Christensen, J. Lauritsen, F. Besenbacher, Phys. Rev. Lett. **100**, 236104 (2008)
19. F. Bocquet, L. Nony, C. Loppacher, T. Glatzel, Phys. Rev. B **78**, 035410 (2008)
20. R. Hoffmann, L. Kantorovich, A. Baratoff, H. Hug, H.J. Güntherodt, Phys. Rev. Lett. **92**, 146103 (2004)
21. R. Hoffmann, C. Barth, A. Foster, A. Shluger, H. Hug, H.J. Güntherodt, R. Nieminen, M. Reichling, J. Am. Chem. Soc. **127**, 17863 (2005)
22. M. Lantz, R. Hoffmann, A. Foster, A. Baratoff, H. Hug, H.R. Hidber, H.J. Güntherodt, Phys. Rev. B **74**, 245426 (2006)
23. R. Hoffmann, D. Weiner, A. Schirmeisen, A. Foster, Phys. Rev. B **80**, 115426 (2009)
24. Y. Sugimoto, P. Pou, M. Abe, P. Jelinek, R. Péerez, S. Morita, O. Custance, Nature **446**, 64 (2007)
25. A. Foster, C. Barth, C. Henry, Phys. Rev. Lett. **102**, 256103 (2009)
26. C. Leendertz, F. Streicher, M.C. Lux-Steiner, S. Sadewasser, Appl. Phys. Lett. **89**, 113120 (2006)
27. S. Burke, J. LeDue, Y. Miyahara, J. Topple, S. Fostner, P. Grütter, Nanotechnology **20**, 264012 (2009)
28. H. Jacobs, P. Leuchtmann, O. Homan, A. Stemmer, J. Appl. Phys. **84**(3), 1168 (1998)
29. J. Colchero, A. Gil, A. Beró, Phys. Rev. B **64**, 245403 (2001)
30. H. McMurray, G. Williams, J. Appl. Phys. **91**(3), 1673 (2002)
31. T. Takahashi, S. Ono, Ultramicroscopy **100**, 287 (2004)
32. E. Palacios-Lidón, J. Abellán, J. Colchero, C. Munuera, C. Ocal, Appl. Phys. Lett. **87**, 154106 (2005)
33. U. Zerweck, C. Loppacher, T. Otto, S. Grafström, L. Eng, Phys. Rev. B **71**, 125424 (2005)
34. U. Zerweck, C. Loppacher, T. Otto, S. Grafström, L. Eng, Nanotechnology **18**, 084006 (2007)
35. K. Wandelt, Appl. Surf. Sci. **111**, 1 (1997)
36. L. Nony, F. Bocquet, C. Loppacher, T. Glatzel, Nanotechnology **20**, 264014 (2009)
37. R. Pérez, I. Stich, M. Payne, K. Terakura, Phys. Rev. B **58**, 10835 (1998)
38. L. Kantorovich, A. Foster, A. Shluger, A. Stoneham, Surf. Sci. **445**, 283 (2000)
39. R. Bennewitz, A. Foster, L. Kantorovich, M. Bammerlin, C. Loppacher, S. Schär, M. Guggisberg, E. Meyer, A. Shluger, Phys. Rev. B **62**(3), 2074 (2000)
40. C. Barth, A. Foster, M. Reichling, A. Shluger, J. Phys. Condens. Matter **13**, 2061 (2001)
41. A. Foster, A. Shluger, R. Nieminena, Appl. Surf. Sci. **188**, 306 (2002)
42. P. Dieska, I. Stich, R. Pérez, Phys. Rev. Lett. **91**, 216401 (2003)
43. W. Hofer, A. Foster, A. Shluger, Rev. Mod. Phys. **75**, 1287 (2003)
44. O. Pakarinen, C. Barth, A. Foster, R. Nieminen, C. Henry, Phys. Rev. B **73**, 235428 (2006)
45. L. Kantorovich, T. Trevethan, Phys. Rev. Lett. **93**, 236102 (2004)
46. T. Trevethan, L. Kantorovich, Nanotechnology **15**, S34 (2004)
47. T. Trevethan, L. Kantorovich, Nanotechnology **15**, S44 (2004)

48. T. Trevethan, L. Kantorovich, J. Polesel-Maris, S. Gauthier, Nanotechnology **18**, 084017 (2007)
49. T. Trevethan, A. Shluger, Nanotechnology **20**, 264019 (2009)
50. T. Trevethan, M. Watkins, L. Kantorovich, A. Shluger, J. Polesel-Maris, S. Gauthier, Nanotechnology **17**, S5866 (2006)
51. Y. Sugimoto, P. Jelinek, P. Pou, M. Abe, S. Morita, R. Perez, O. Custance, Phys. Rev. Lett. **98**, 106104 (2007)
52. T. Trevethan, M. Watkins, L. Kantorovich, A. Shluger, Phys. Rev. Lett. **98**, 028101 (2007)
53. T. Trevethan, L. Kantorovich, J. Polesel-Maris, S. Gauthier, A. Shluger, Phys. Rev. B **76**, 085414 (2007)
54. N. Martsinovich, L. Kantorovich, Phys. Rev. B **77**, 205412 (2008)
55. T. Trevethan, A. Shluger, J. Phys. Chem. C **112**, 19577 (2008)
56. M. Watkins, T. Trevethan, M. Sushko, A. Shluger, J. Phys. Chem. C **112**, 4226 (2008)
57. L. Nony, A. Foster, F. Bocquet, C. Loppacher, Phys. Rev. Lett. **103**, 036802 (2009)
58. L. Nony, A. Baratoff, D. Schär, O. Pfeiffer, A. Wetzel, E. Meyer, Phys. Rev. B **74**, 235439 (2006)
59. M. Gauthier, R. Pérez, T. Arai, M. Tomitori, M. Tsukada, Phys. Rev. Lett. **89**(14), 146104 (2002)
60. G. Couturier, R. Boisgard, L. Nony, J.P. Aimé, Rev. Sci. Instrum. **74**(5), 2726 (2003)
61. G. Couturier, R. Boisgard, D. Dietzel, J.P. Aimé, Nanotechnology **16**, 1346 (2005)
62. J. Polesel-Maris, S. Gauthier, J. Appl. Phys. **97**, 044902 (2005)
63. J. Kokavecz, Z. Toth, Z. Horvath, P. Heszler, A. Mechler, Nanotechnology **17**, S173 (2006)
64. C. Loppacher, M. Bammerlin, F. Battiston, M. Guggisberg, D. Müller, H.R. Hidber, R. Lüthi, E. Meyer, H.J. Güntherodt, Appl. Phys. A **66**, S215 (1998)
65. R.E. Best, *Phase Locked Loops: Design, Simulation and Applications*, 4th edn. (Mc Graw-Hill, New York, 1999)
66. M. Guggisberg, M. Bammerlin, C. Loppacher, O. Pfeiffer, A. Abdurixit, V. Barwich, R. Bennewitz, A. Baratoff, E. Meyer, H.J. Güntherodt, Phys. Rev. B **61**, 11151 (2000)
67. D. Rapaport, *The Art of Molecular Dynamics Simulation* (Cambridge University Press, Cambridge, 1995)
68. R. Watson, J. Davenport, M. Perlam, T. Sham., Phys. Rev. B **24**, 1791 (1981)
69. A. Shluger, A. Rohl, D. Gay, R. Williams, J. Phys. Condens. Matter **6**, 1825 (1994)
70. A. Schirmeisen, D. Weiner, H. Fuchs, Phys. Rev. Lett. **97**, 136101 (2006)
71. F.J. Giessibl, Phys. Rev. B **61**, 9968 (2000)
72. L. Gross, F. Mohn, P. Liljeroth, J. Repp, F. Giessibl, G. Meyer, Science **324**, 1428 (2009)